

Improved Accident Tolerance of Austenitic Stainless Steel Cladding through Colossal Supersaturation with Interstitial Solutes

Fuel Cycle Research and Development

Frank Ernst

Case Western Reserve University

In collaboration with:

University of Akron

Frank Goldner, Federal POC
Mychailo Toloczko, Technical POC

Improved Accident Tolerance of Austenitic Stainless Steel Cladding through Colossal Supersaturation with Interstitial Solutes

F ERNST,¹ R LILLARD,² and S. MALOY³

¹*Department of Materials Science and Engineering, Case Western Reserve University, 10900 Euclid Avenue, Cleveland, Ohio 44106-7204.*

²*Department of Chemical and Biomolecular Engineering, University of Akron, Akron OH 44325-3906.*

³*Los Alamos National Laboratory, Los Alamos, NM 87545.*

(October 17, 2016)

I. INTRODUCTION

A. Goals

We proposed a program-supporting research project in the area of fuel-cycle R&D, specifically on the topic of advanced fuels. Our goal was to investigate whether SECIS (surface engineering by concentrated interstitial solute – carbon, nitrogen) can improve the properties of austenitic stainless steels and related structural alloys such that they can be used for nuclear fuel cladding in LWRs (light-water reactors) and significantly excel currently used alloys with regard to performance, safety, service life, and accident tolerance.

The concept of SECIS consists of dissolving very high concentrations of interstitial solute, typically orders of magnitude higher than the solubility limit, within a (e.g. 25 μm thick) layer below the alloy surface. This can provide substantial “case hardening” (i.e. generate a hard shell). Particularly if precipitation of the solute or its compounds can be avoided, many other properties can also be tremendously improved, e.g. the wear resistance, fatigue resistance, and corrosion resistance. In this project, we intended to demonstrate that SECIS can be adapted for post-processing of clad tubing to significantly enhance mechanical properties (hardness, wear resistance, and fatigue life), corrosion resistance, resistance to stress-corrosion cracking (hydrogen-induced embrittlement), and – potentially – radiation resistance (against electron-, neutron-, or ion-radiation damage). As SECIS can be applied as a highly conformal post process to components in their final shape – without changing their dimensions – and at low cost, our expectation was that this technology can make a valuable contribution for developing better, safer, longer-lasting, and more accident-tolerant fuel cladding. To test this hypothesis, we measured various relevant properties of the surface-engineered alloys and compared them with corresponding properties of the non-treated, as-received alloys. In particular, we studied the impact of heat exposure corresponding to BWR (boiling-water reactor) working- and accident (loss-of-coolant) conditions and the effect of ion irradiation.

B. Approach

1. Processing

One method of SECIS that has been subject to intense research at CWRU (Case Western Reserve University) for more than one decade is LTC (low-temperature carburization). The initial focus of that research was a *gas-phase* process for LTC, empirically developed specifically for AISI-316L (austenitic stainless steel) by Swagelok. The underlying physical principle of LTC is to let carbon diffuse into the alloy surface at a processing temperature T_p that effectively freezes diffusion of metal atoms (Fe, Cr, Ni), such that no precipitation of e.g. Cr-rich carbides can occur within the processing time. On the other hand, T_p is still high enough to enable transport of carbon into technically useful depths below the alloy surface ($\zeta \approx 25 \mu\text{m}$) within technically feasible processing times $t_p = 0.1 \text{ Ms}$. The difference between this novel approach to conventional high-temperature carburization is illustrated in the TTT (time-temperature-transformation) diagram of Fig 1.

Most critical for successful LTC is the removal of the $\approx 1 \text{ nm}$ thick Cr-rich passivating oxide layer from the surface of AISI-316L. This “surface activation” is important as the oxide layer, which makes the alloy “stainless,” is not transparent to carbon at T_p . In the CGP (conventional gas-phase) process for LTC, industrially employed by Swagelok, surface activation is accomplished by exposing the alloy surface to HCl gas before the actual carburization. Subsequently, the actual LTC is accomplished with the help of CO in a carrier gas consisting of N_2 (the N_2 molecule is so stable that the carrier gas does not provide any diffuse into the alloy).

Later, the scope of research was broadened to include further structural alloys, e.g. AL-6XN (Allegheny Ludlum, superaustenitic stainless steel) or IN-718 (Inconel, Ni-superalloy), to experiment with further methods of surface activation (e.g. using acetylene), and to include nitrogen as alternative or additional interstitial solute for LTN (low-temperature nitridation) or LTNC (low-temperature nitro-carburization), respectively.

Initially, we set out to experiment with three different alloys: AISI-316L, IN-718, and AL-6XN (Table I). Our

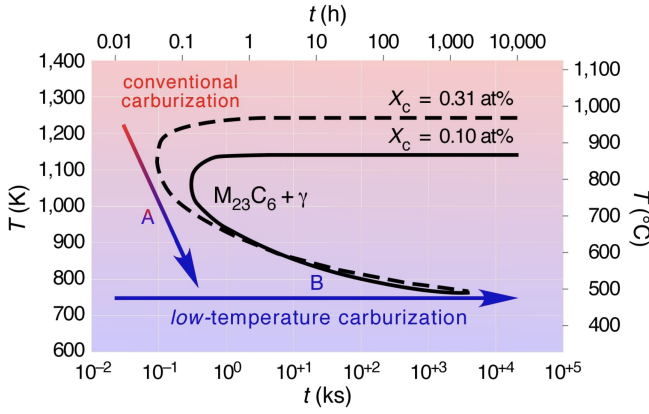


FIG. 1: TTT diagram illustrating the concept of LTC. The “C” curves correspond to two different austenitic stainless steels. It can be seen that increasing the carbon content moves the “C” curve (“pearlite nose”) to the upper left, implying that very high – industrially entirely unfeasible – quench rates would be needed for common fractions $X_C \approx 0.1 = 10\%$. The approach of LTC is to operate at a temperature $T_p = \text{const.}$ at which the carbide precipitation described by the “C” curves is kinetically suppressed, i. e. will not occur within the processing time t_p . On the other hand, T_p is still high enough to enable considerable transport of carbon into the alloy.

TABLE I: Alloy Atom Fractions

	AISI-316L Coupon	AISI-316L Tube	IN-718 Coupon	IN-718 Tube	AL-6XN Coupon
Fe	0.6928	0.6825	0.1914	0.1932	0.4308
Cr	0.1942	0.1772	0.2111	0.1997	0.2396
Ni	0.0955	0.1087	0.5167	0.5240	0.2461
Al			0.0107	0.0124	
C		0.001	0.0019	0.0025	0.0014
Cu		0.0012	0.0014	0.0007	
Mn		0.0173	0.0019	0.0024	0.0206
Mo	0.0175	0.0121	0.0184		0.0413
Nb			0.0319	0.0315	
Si			0.0037	0.0018	0.0202
Ti			0.0109	0.0118	

goal was to adapt the Swagelok process to work with tubes with the shape and dimensions that are used for nuclear fuel cladding (Table II). In the course of the project, we discovered a more elegant method of processing that yields better results than the Swagelok process with shorter processing times t_p : LTNC by SRP (solid-reagent pyrolysis). Instead of separately activating the alloy surface and infusing interstitial solute, this method works by encapsulating the work-piece together with a solid reagent (powder), e. g. in an evacuated fused-silicon ampoule. Upon heating, the reagent pyrolyzes into a gas containing molecular species that both activate the surface and provide

TABLE II: Dimensions of Tube Specimens

Outer diameter (mm)	10.00
Inner diameter (mm)	9.45
Wall thickness (mm)	0.33
Length (mm)	140.00

carbon and nitrogen to diffuse into the alloy.

In the first phase of the project, we focused on AISI-316L and how to adapt the Swagelok process to work with tubes. Then, we discovered and began to develop LTNC of SRP, first for AISI-316L. In the second phase, we shifted focus on IN-718 and recognize that this is the most promising alloy for the targeted application. To further develop LTNC by SRP and fully explore the potential of IN-718, we reduced the workscope for AL-6XN.

2. Benefits of SECIS Under Reactor Conditions

Based on earlier work, it was expected that SECIS of the structural alloys under consideration would greatly improve their standard mechanical properties (surface hardness, wear resistance, fatigue resistance) and corrosion resistance under ambient conditions. These substantial benefits of SECIS were confirmed in the current study. In particular, the exceptional increase of corrosion resistance that LTC provides for AISI-316L has been investigated in detail in the recent joint publication of UA (University of Akron) and CWRU.¹ However, for nuclear power applications, and in particular for accident tolerance, it is also of great interest how SECIS impacts alloy response to heat exposure, high-temperature *steam* exposure, corrosion resistance in hot water, resistance to SCC (stress-corrosion cracking) under simulated BWR conditions, and proton- or ion irradiation. Therefore, we have carried out systematic studies in which we have compared the response of SECIS-treated alloys with that of corresponding non-treated alloys.

II. SUMMARY OF EXPERIMENTAL ACTIVITIES

A. Processing

1. SECIS of all alloys was performed at CWRU, as well as supporting optical metallography and microcharacterization using XRD (X-ray diffractometry), SEM (scanning electron microscopy), SAM (scanning Auger microprobe), AFM (atomic force microscopy), MFM (magnetic force microscopy), and TEM (transmission electron microscopy).

2. For reproducing the Swagelok process for LTC at CWRU and extending it to LTN and LTNC, we employed a computer-controlled gas furnace made by CVD.

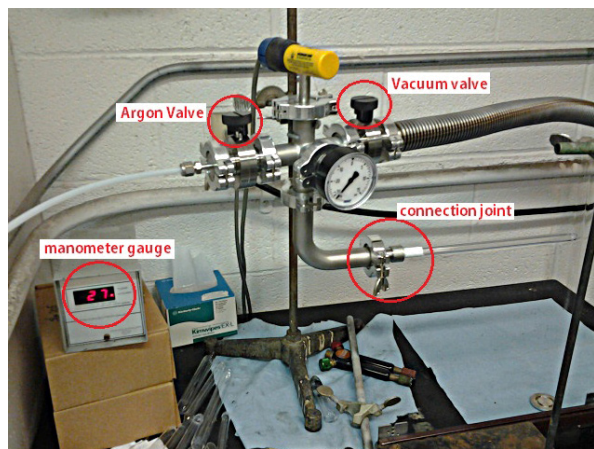


FIG. 2: Encapsulation station, constructed for encapsulating specimens together with SRP (solid-reagent pyrolysis) in evacuated fused-silica ampoules.

3. For SRP processing, we designed and constructed an encapsulation station (Fig 2) suitable to encapsulate alloys specimens together with solid-reagent powders of different compositions in evacuated fused-silica ampoules. The ampoules were heat-treated in a number of different furnaces at CWRU.

B. Surface Hardness and Wear Testing

CWRU performed surface hardness testing using a Vickers microhardness tester and nanoindenters. Ball-on-disk testing was performed using a commercial wear station. Coupons of LTC AISI-316L were exposed to wear testing and compared to corresponding non-treated material. The tests were conducted as ball-on-plate linear-motion dry wear tests in air with a load of 1 kg and a duration of 1 ks. These conditions correspond to ASTM G133, except for the load, which was adjusted to obtain meaningful results. Acquired test data included the surface profile of the wear scar and the worn volume.

C. Corrosion Testing Under Simulated BWR Conditions

For corrosion testing under simulated BWR conditions, specimens were exposed for long-term in the newly constructed autoclave system installed at UA at the beginning of the project. The system is equipped with circulated water flow at elevated temperature. The purpose is to maintain realistic oxygen activity; in non-circulating water, the oxygen activity would decrease as metal parts get the available oxygen. Corrosion rates were monitored by measuring the weight specimens at different stages of the experiment.

D. Slow-Strain-Rate Tensile Testing

UA performed tensile testing (i) under ambient conditions, that is in air at room temperature, and (ii) under

simulated BWR conditions.

Simulated BWR conditions were set up in an autoclave system that was installed at UA at the beginning of the project particularly for this purpose. The experiments were carried out with water of “normal” chemical composition (less driving force for SCC than e. g. hydrogenated water). The water was circulated to maintain normal oxygen activity (in non-circulating water, the oxygen activity would decrease as metal parts get the available oxygen). The system is properly protected against galvanic coupling of dissimilar metal parts. Simulated BWR conditions were set up with a temperature $T = 561 \text{ K}$ (288°C) and a pressure $p = 17 \text{ MPa}$ (2400 psi, $\approx 170 \text{ atm}$). Under these conditions, the water is just below the critical temperature and just above the critical pressure for steam formation.

Under ambient as well as under simulated BWR conditions, specimens were strained low rates of $\dot{\epsilon} = 1 \cdot 10^{-6} \text{ s}^{-1}$. In all tests, the specimens were cylinders with a diameter of 3.2 mm.

E. Exposure to Heat and Irradiation

Under normal operating conditions of a BWR, fuel cladding can be exposed to temperatures of $T_0 = 620 \text{ K}$ (350°C) and, at the same time, high flux rates of irradiation (e. g. proton or ion irradiation). While $T_0 < T_p$, the diffusivity of the interstitial solute will be higher than at room temperature. After prolonged time at T_0 , diffusion might flatten the fraction-depth profile $X[z]$ of the interstitial solute (e. g. carbon) to decrease the beneficial effects brought about by high fractions of interstitial solute in the beginning.

Irradiation, e. g. by high-energy protons or ions, generally causes effects similar to the increased diffusivity enabled by elevated temperature. To study the impact of such exposure on SECIS-treated AISI-316L and IN-718, and to discriminate between the effects of just heat versus heat and irradiation, we have performed heat exposure experiments at $T_0 = 620 \text{ K}$ for $t_0 = 84 \text{ ks}$ (1 d) in air as well as combined exposure to heat and irradiation with high-energy protons or Ni^{+2} ions. These experiments were performed at LANL (Los Alamos National Laboratory).

Under the conditions of an accident, alloy parts might be exposed to much higher temperatures and steam. To model such a condition, we have assumed an exposure to $T_a = 1073 \text{ K}$ (800°C) for $t_a = 3.6 \text{ ks}$ (1 h). Corresponding high-temperature steam exposure experiments were also performed at LANL. As the conditions simulating an accident are harsh, corresponding alloy specimens were first exposed to just the temperature – without steam – in air and in vacuum at CWRU.

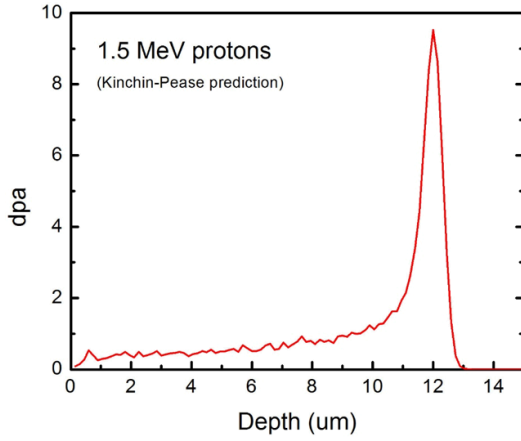


FIG. 3: Profile $\phi[z]$ of proton irradiation (in units of dpa – displacements per atom) that was applied to AISI-316L engineered by CGP LTNC and an NSE (non-surface-engineered) reference specimen. $\phi[z]$ is the depth-density of the average number of displacements per atom (in units of “dpa” – displacements per atom).

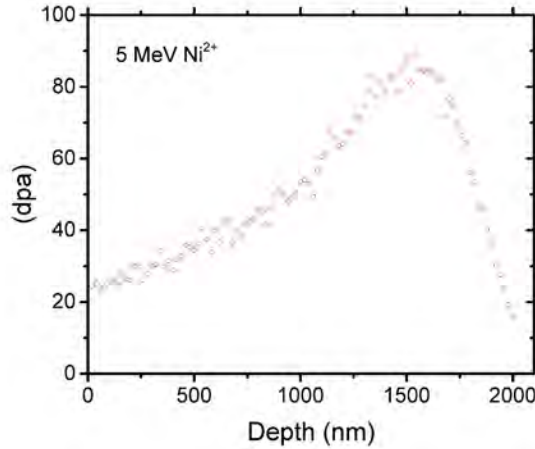


FIG. 4: Profile $\phi[z]$ of Ni^{2+} ion irradiation that was applied to IN-718 engineered by CGP LTNC and an NSE (non-surface-engineered) reference specimen.

F. Irradiation

Part of our project was to carry out first experiments on the response of SECIS-engineered alloys to irradiation with high-energy protons and ions.

Proton irradiation was carried out on CGP LTC AISI-316L and an NSE (non-surface-engineered) AISI-316L reference specimen. The experiment was conducted with 1.5 MeV protons. The total dose corresponded to 0.5 dpa, i.e. a displacement of every other atom on the average within the affected zone. The temperature was held at 620 K (350 °C). Figure 3 shows the profile $\phi[z]$ of proton irradiation, which corresponds to the depth-density of the average number of displacements per atom (in units of “dpa” – displacements per atom). The

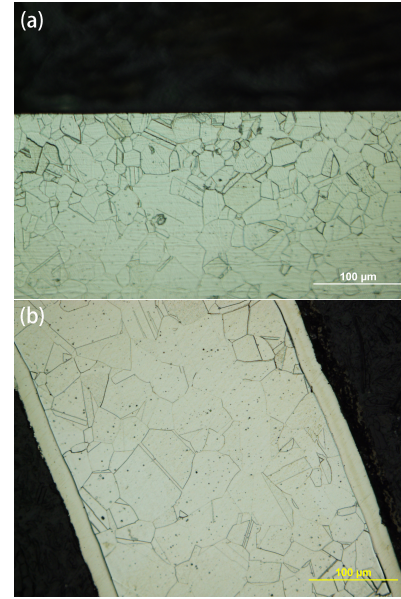


FIG. 5: LOM (light-optical microscopy) of cross-sectional AISI-316L specimens after polishing and etching. (a) NSE coupon, as-received. (b) Tube after LTC (low-temperature carburization). The $\approx 25 \mu\text{m}$ thick zone below the surface is the carbon-rich case.

graph shows $\phi[z]$ fairly uniform over the first 10 μm of depth z , then peaks at around 12 μm . The $\phi[z]$ graph was calculated using Kinchin-Pease formalism. During this irradiation a new PIXE (particle-induced X-ray emission) technique for automatic particle counting was implemented. This method provided a more accurate charge integration and therefore more accurate dose calculation. After irradiation, TEM (transmission electron microscopy) specimens were prepared by FIB (focused ion beam).

IN-718 engineered by CGP LTNC and an NSE reference specimen were exposed to irradiation with 5 MeV Ni^{2+} . The corresponding $\phi[z]$ is shown in Fig 4. During the irradiation, the temperature was held at the same temperature of 620 K (350 °C), as in the proton irradiation experiment. Again, $\phi[z]$ was calculated using Kinchin-Pease formalism, and the new PIXE technique was used again for automatic particle counting.

III. SUMMARY OF RESULTS

A. Processing

1. CGP LTC in a computer-controlled gas furnace has been successfully adapted for tubes as used for nuclear fuel cladding. Resolved problems include the effect of the microstructure that results from tube manufacturing as well as compensating for effects related to increased gas flow resistance on the inside of tubes compared to flow resistance on the outside.

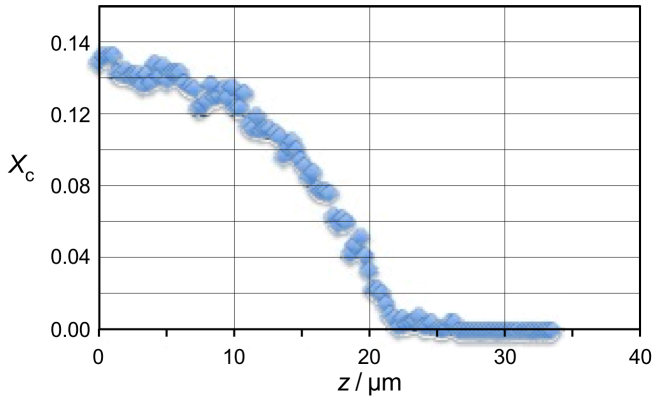


FIG. 6: Carbon-concentration-depth profile $X_C[z]$ for AISI-316L treated by CGP LTC.

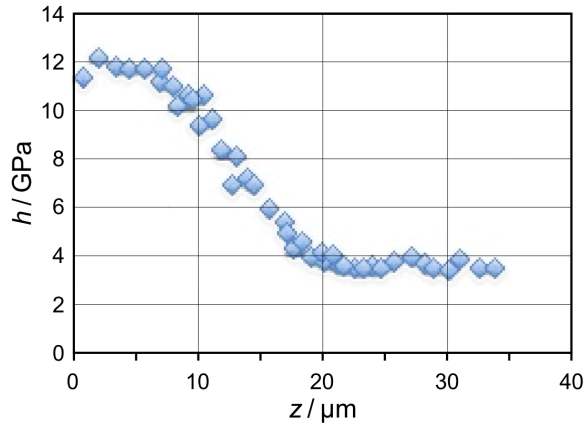


FIG. 7: Microhardness-depth profile $h[z]$ for AISI-316L treated by CGP LTC.

2. Processing parameters were developed for LTC, LTN, and LTNC of AISI-316L and IN-718 tubes. Figure 5b shows an example of a light-optical micrograph of a polished and etched metallographic cross-section of an CGP LTC AISI-316L tube.

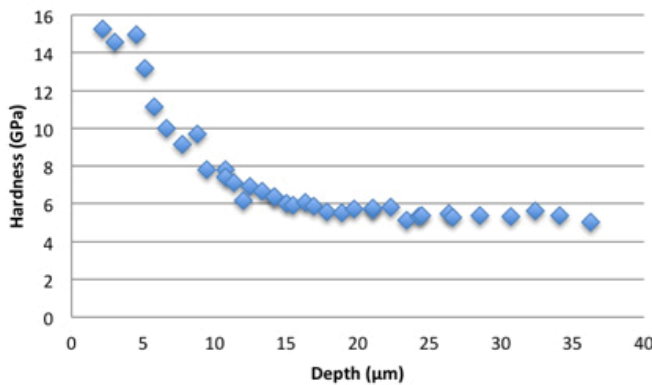


FIG. 8: Nanohardness-depth profile $h[z]$ LTC IN-718.

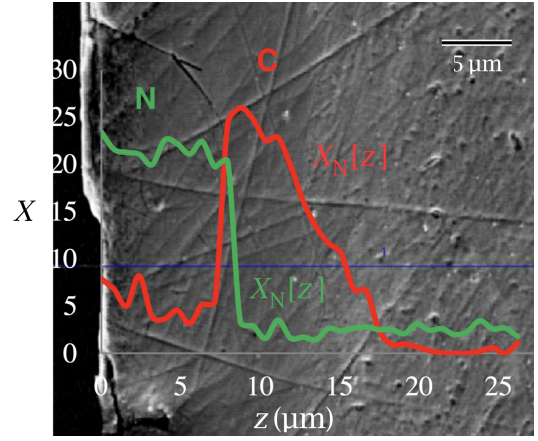


FIG. 9: LTNC of IN-718 by SRP. Carbon- and nitrogen-fraction-depth profiles $X_C[z]$ (red) and $X_N[x]$ (green).

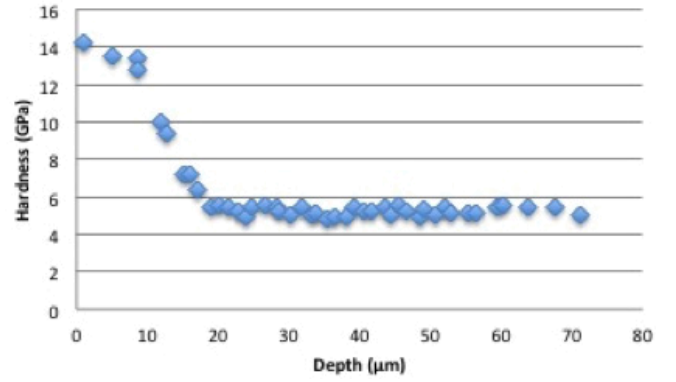


FIG. 10: Nanohardness-depth profile $h[z]$ for IN-718 treated by CGP LTNC.

3. Case depths ζ of order 25 μm are obtained within processing times of $t_p \approx 80$ ks. An example of a typical carbon-fraction-depth profile $X_C[z]$ in LTC AISI-316L is shown in Fig 6. An example of LTC IN-718 is shown in Fig 9.

4. Substantial increases in surface hardness were obtained, with hardness-depth profiles $h[z]$ corresponding to the interstitial-fraction-depth profiles. An example of $h[z]$ for CGP LTC AISI-316L is shown in Fig 7. An example of $h[z]$ for IN-718 treated by CGP LTNC is shown in Fig 10.

5. A surprising result for IN-718 was that the case generated by CGP LTNC is *ferromagnetic*. The ferromagnetic behavior was observed by macroscopic interaction with permanent magnets as well as by MFM (*magnetic-force microscopy*), Fig 11.

6. For LTNC by SRP, we designed and constructed an encapsulation station.

7. With regard to the conventional gas-phase processing in a computer-controlled gas furnace, we discovered that surface activation of AISI-316L and AL-6XN

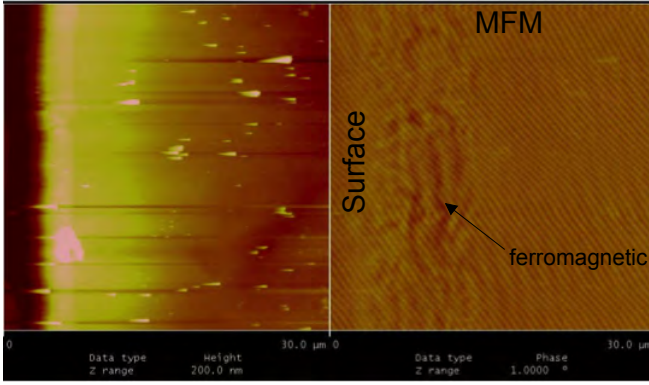


FIG. 11: MFM (magnetic-force microscopy) image of IN-718 treated by CGP LTNC. The left-hand side shows a topographic image (alloy surface vertical on the left), whereas the actual MFM image of the same region is shown on the right. In the MFM image, the sinusoidal modulations parallel to the left edge indicate a magnetic domain structure that is typical of ferromagnetism.

can be accomplished by *external* treatment in *liquid* HCl (instead of gaseous HCl in the furnace), followed by a drying procedure that effectively passivates the alloy surface against re-oxidation, maintaining it transparent to carbon and nitrogen for several hours.

8. Successful SECIS by conventional gas-phase LTC and LTN in a computer-controlled furnace was accomplished for three alloys, AISI-316L, IN-718, and AL-6XN, as indicated in Table III.

9. For CGP SECIS of *tubes*, we found that it may be necessary to take specific measures to increase the gas flow in the interior of the tube. Otherwise, according to the Hagen-Poiseuille law, the increased resistance of the tube interior to gas flow may prevent adequate gas supply on the inside.

10. SECIS by SRP in evacuated fused-silica ampoules was accomplished with impressive results for AISI-316L and IN-718. Figure 9 shows an example of IN-718. After LTNC for only 7.2 ks (2 h), a case has already formed with a depth $\zeta > 15 \mu\text{m}$. Interestingly, the case consists of a nitrogen-rich layer on the outside (alloy surface) and a carbon-rich layer on the inside (below). The apparent “uphill” diffusion of carbon has its explanation in the effect of nitrogen increasing the chemical potential μ_c of carbon. The driving force for diffusion is the chemical-potential gradient $\partial_z \mu_c$, not the concentration gradient $\partial_z X_C$, and the chemical potential μ_c actually does decrease monotonously with increasing z : $\partial_z \mu_c < 0$ for all $z > 0$. Details of the processing conditions, including the results of challenging *in situ* gas pressure measurements, can be found in a recently published MS thesis.²

TABLE III: Methods of SECIS Established for Different Alloys

	LTC	LTN	LTNC
AISI-316L	✓	✓	✓
IN-718	✓	✓	✓
AL-6XN	✓		

B. Surface Hardness

As expected on the basis of prior work, the mechanical tests performed at CWRU indicate significant surface hardness increase for all SE-IS-engineered alloys, regardless of the alloy, specimen shape (tube, coupon, cylinder) particular species of infused solute and processing method (conventional gas-phase LTC or -LTN or SRP-based LTNC).

C. Wear Resistance

As expected, SECIS by LTC dramatically improves the wear resistance. For AISI-316L, for example, the wear scar is obvious for non-treated 316L coupons, but barely visible on the surface-engineered coupon. Quantitatively, LTC reduces the worn volume of AISI-316L by a factor of ≈ 100 .

D. Corrosion Resistance

SECIS by LTC, LTN, and LTNC generally significantly improves corrosion resistance under ambient conditions. Specifically, our work has shown that LTC, LTN, and LTNC significantly improves the corrosion resistance of AISI-316L in saltwater and under conditions of metallographic etching. Experimental data demonstrating this finding are shown in Fig 12.

Under simulated BWR conditions, however, NSE and SECIS AISI-316L and IN-718 responded with similar corrosion rates. After exposing corresponding samples in the re-circulating autoclave at 560 K (288 °C) for 1.8 Ms 500 h, analysis of mass loss did not reveal any significant difference in corrosion rates between NSE and SECIS samples.

E. Slow-Strain-Rate Tensile Testing

1. AISI-316L

For AISI-316L, only specimens treated by CGP LTC and NSE specimens were tested in tension. Fig 14 shows the measured $\sigma[\epsilon]$ curves of the flow stress as a function of strain. Under ambient conditions, as seen in the LTC-treated specimen exhibited significantly reduced strain to failure and - unexpectedly - significantly higher YS (yield stress) σ_y ($:= \sigma[\epsilon]|_{\epsilon=0.2}$), UTS (ultimate tensile strength) σ_s , and flow stress $\sigma[\epsilon]$ over the entire ϵ range. This strong effect of LTC is remarkable as the fraction of the carburized cross section is only $\approx 0.25\%$ of the total cross-section.

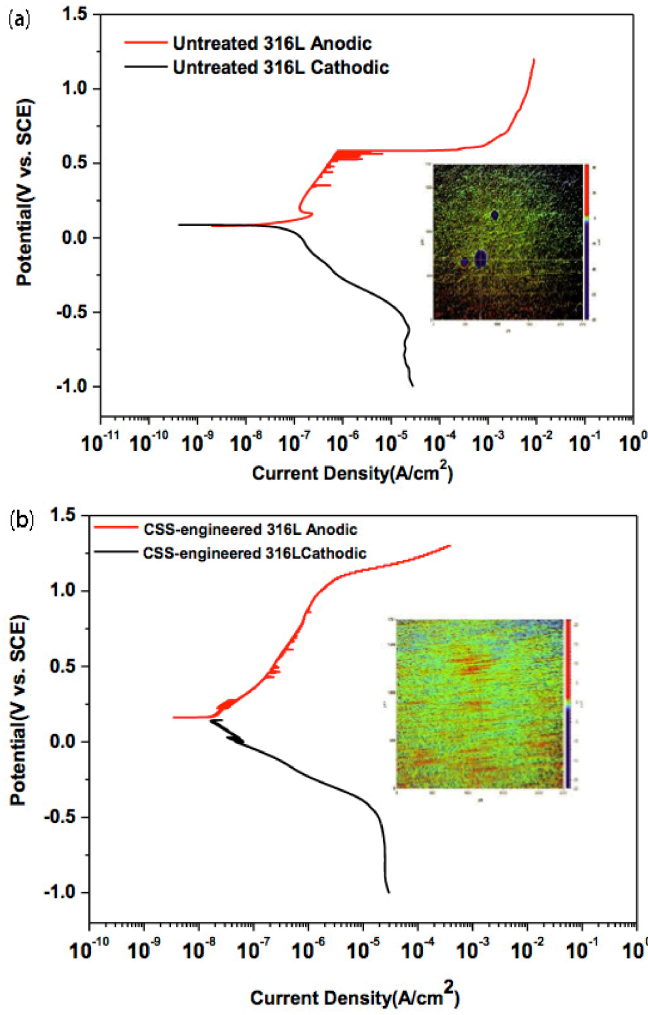


FIG. 12: Polarization curves demonstrating the improvement of corrosion resistance in 0.1 M NaCl obtained by LTC. (a) NSE AISI-316L. (b) AISI-316L engineered by CGP LTC.

Under simulated BWR conditions, the main difference is a reduction in strain to failure, ϵ_f , to $\approx 1/2$. Different from slow-strain-rate testing in air, no significant effect of LTC is observed on σ_y , nor σ_s , nor $\sigma[\epsilon]$ (for $\epsilon < \epsilon_f$). Again, the effect of LTC on ϵ_f is quantitatively much larger than might be expected from the very small fraction ($\approx 0.25\%$) of the carburized cross-section in the total cross-section. This means that the significantly reduced ϵ_f is not an effect of mechanical weakness in the carburized layer alone. Rather, the carburized layer appears to *induce* SCC in the non-carburized alloy core. As illustrated in Fig 13, the reduced ductility of the carbon-rich layer (case) needs to propagation of cracks into substantial depths of the non-carburized alloy core. As a result, ductile overload occurs in the central part of the specimen cylinder, eventually causing rupture.

The difference in microscopic slow-strain failure mechanisms between air exposed LTC AISI-316L and

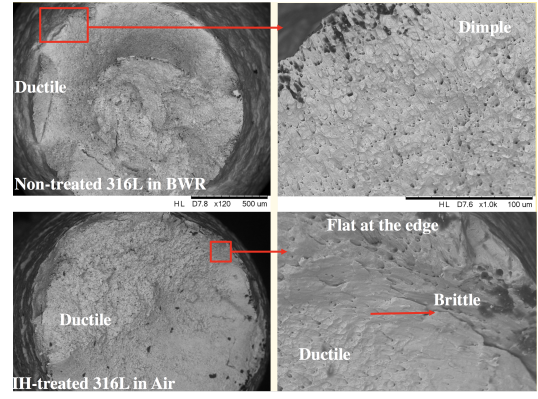


FIG. 13: Slow-strain-rate tensile deformation of AISI-316L – microscopic mechanisms revealed by SEM (scanning electron microscopy). (a) In air. (b) Under simulated BWR conditions.

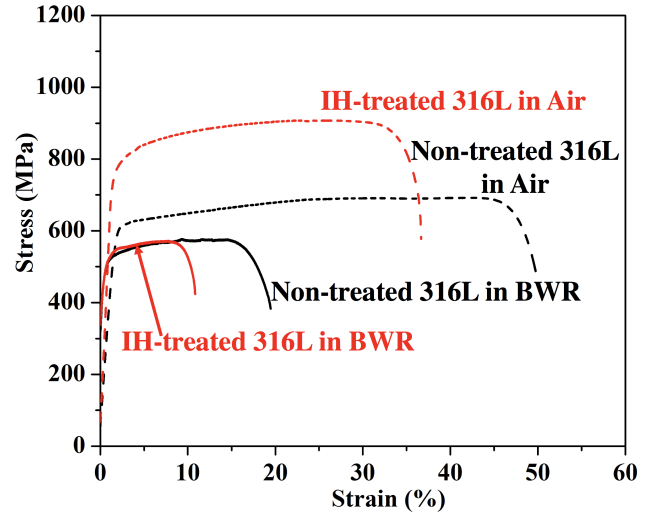


FIG. 14: Stress-strain curves obtained by tensile tests.

material exposed to simulated BWR conditions is revealed by Fig 13. In both cases, tensile strain causes cracking of the (less ductile) case. However, while the ductile alloy core stops crack propagation in air, it fails to do so under simulated BWR conditions.

2. IN-718

More promising results were obtained with SECIS of IN-718, treated by LTC or LTNC. Figure 16 presets a comparison of stress-strain curves obtained from comparative tensile testing of LTC versus NSE IN-718 in air and under simulated BWR conditions. These curves show hardly any difference. The only remarkable feature is that ϵ_f is slightly larger for simulated BWR conditions than in air – both for LTC and NSE. Summarizing, it appears that LTC neither compromises, nor improves SCC of IN-718.

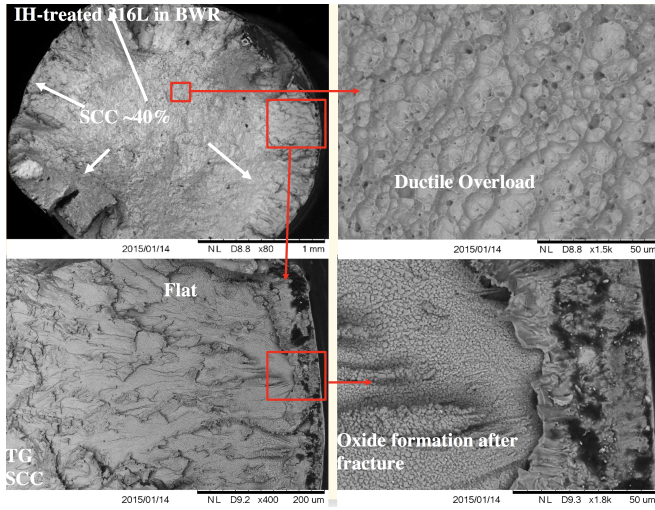


FIG. 15: SEM (scanning electron microscopy) fractographs of AISI-316L after tensile rupture in simulated BWR environment.

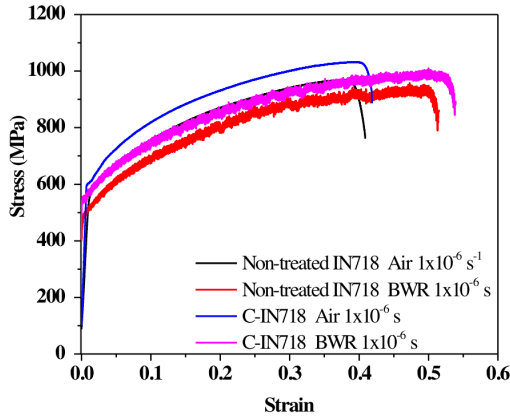


FIG. 16: Tensile testing of IN-718: Stress-strain curves for LTC versus NSE IN-718 in air and under simulated BWR conditions.

3. Discussion of SCC

SECIS, and in particular LTC, LTN, or LTNC, induces very high (GPa-level) biaxial residual compressive stress in the case layer. Measured values for AISI-316L treated by LTC are $\sigma^{11} = \sigma^{22} = 2$ GPa. The biaxial compressive stress is generally beneficial for mechanical properties. For example, have observed that LTC of AISI-316L prolongs the high-cycle fatigue life by a factor of ≈ 100 . The physical interpretation is that the compressive stress does not allow the usual nucleation of fatigue cracks at the specimen surface; the stress will tend to close any cracks that might have formed under ordinary conditions.

Similar effects are expected for SCC, as illustrated in Fig 17.

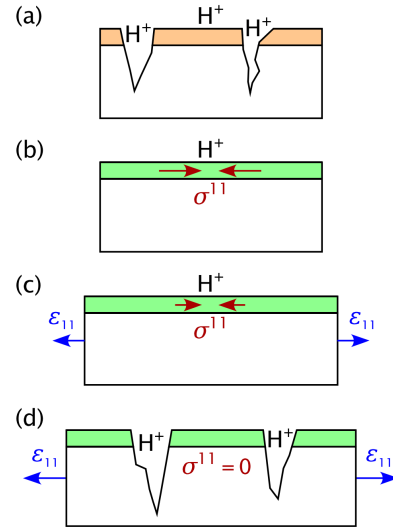


FIG. 17: SCC crack nucleation in case-hardened alloys - effect of biaxial residual compressive stress. (a) Absent compressive stress, uniaxial tensile strain on SCC may induce crack nucleation in the case (hard shell), as increased hardness implies reduced ductility. Although the core is more ductile than the case, cracks can propagate into the core if *corrosion* (e.g. via protons) in the alloy core progresses more rapidly than dislocation activity can blunt the crack tip. (b) SECIS leaves the surface under *biaxial compressive residual stresses* σ^{kk} ($k = 1, 2$), which tend to close cracks. (c) Uniaxial tensile strain ϵ_{11} parallel to the surface reduces σ^{kk} . (d) Increasing ϵ_{11} , $\sigma^{kk} \rightarrow 0$ and the surface becomes susceptible to the formation of sharp cracks in the case - as seen in Fig. 15.

F. Normal-Heat Exposure

To simulate heat exposure under normal, i.e. operating conditions, SECIS-treated specimens of AISI-316L, AL-6XN, and IN-718 were exposed to $T_0 = 620$ K for $t_0 = 84$ ks (1 d) in air. The important answer we expected from these experiments was the change of the fraction-depth profile $X_C[z]$ of the interstitial solute and corresponding changes in the hardness-depth profile $h[z]$.

For IN-718 engineered by CGP LTC, the profile $X_C[z]$ in Fig 18 shows no significant difference to the original profile shown in Fig 6. For IN-718 engineered by CGP LTNC, Fig 19 shows that the heat treatment hardly changes the case thickness $\zeta \approx 20$ μ m. Similarly, the hardness-depth profile $h[z]$ in Fig 20 is effectively identical to the profile before the heat treatment, shown in Fig 8. The absence of change in $h[z]$ also indicates absence of carbide precipitation. Accordingly, the extent to which carbon diffusion occurs during the heat treatment is negligible. A similar stability of the concentration-depth profile $X_C[z]$ was observed for AL-6XN, as shown in Fig 21. Also for this alloy, normal heat exposure did not cause any carbide precipitation detectable by XRD (X-ray diffractometry) (Fig 22).

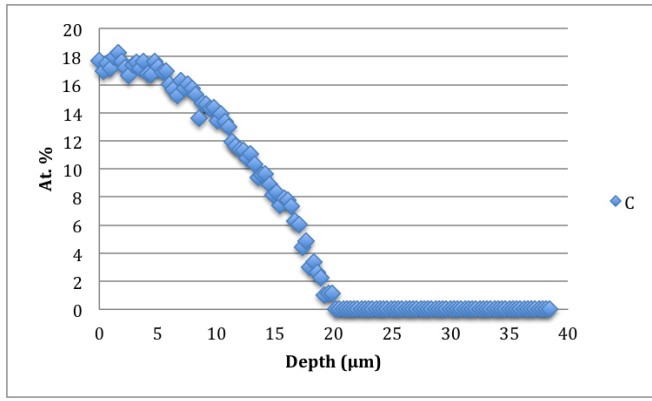


FIG. 18: Carbon-fraction-depth profile $X_C[z]$ of LTC AISI-316L after 86.4 ks at 620 K.

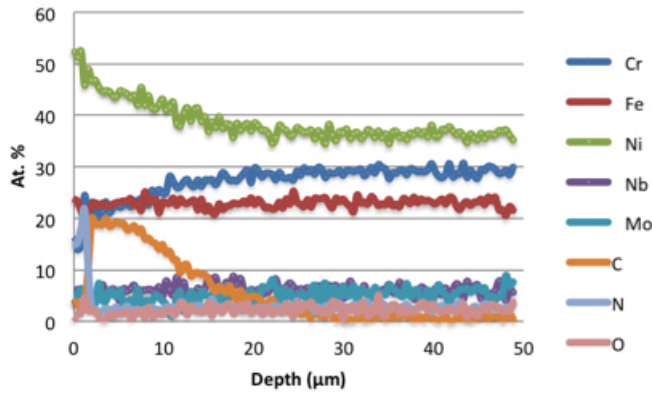


FIG. 19: Atom-fraction-depth profiles $[z]$ of CGP LTNC IN-718 after 86.4 ks at 620 K.

G. High-Temperature Steam Exposure

To simulate *accident* conditions in nuclear applications, HTSE (*high-temperature steam exposure*) was performed at 1073 K (800 °C) for 3.6 ks (1 h). These experiments were carried out at LANL, however only for IN-718 - SECIS-treated by LTC and LTNC. The initial plan of performing these experiments also on AISI-316L had to be given up because with that alloy, the case formed by LTC or LTNC was already completely

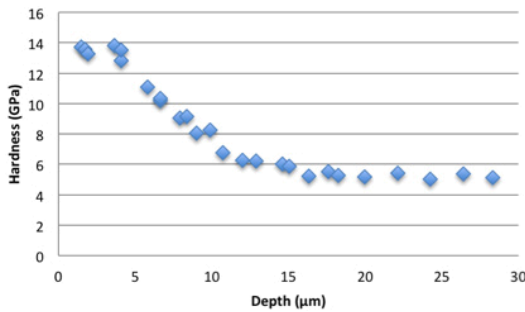


FIG. 20: Nanohardness-depth profile $h[z]$ LTC IN-718 after 86.4 ks at 620 K.

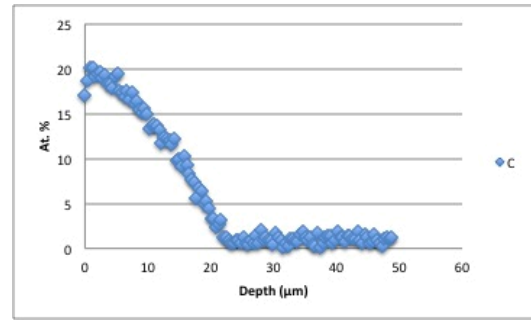


FIG. 21: Atom-fraction-depth profiles $X_C[z]$ of CGP LTC AL-6XN before (blue) and after (red) 86.4 ks at 620 K.

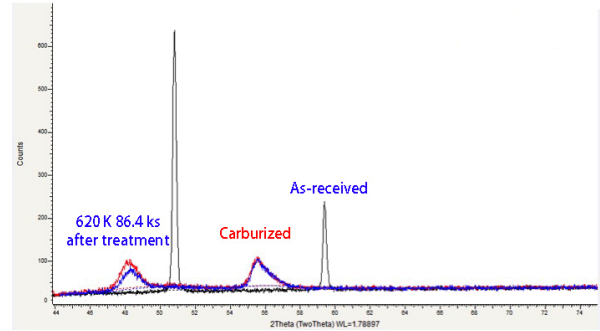


FIG. 22: X-ray diffractograms of CGP LTNC AL-6XN after 86.4 ks at 620 K.

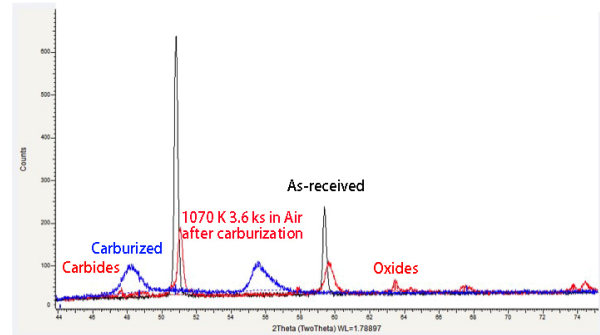


FIG. 23: X-ray diffractograms of CGP LTNC AL-6XN after 3.6 ks at 1073 K in air.

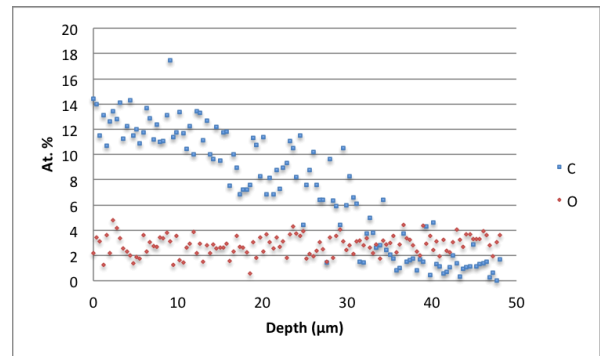


FIG. 24: Atom-fraction-depth profiles $X_C[z]$ of CGP LTC AL-6XN after 3.6 ks at 1070 K in vacuum.

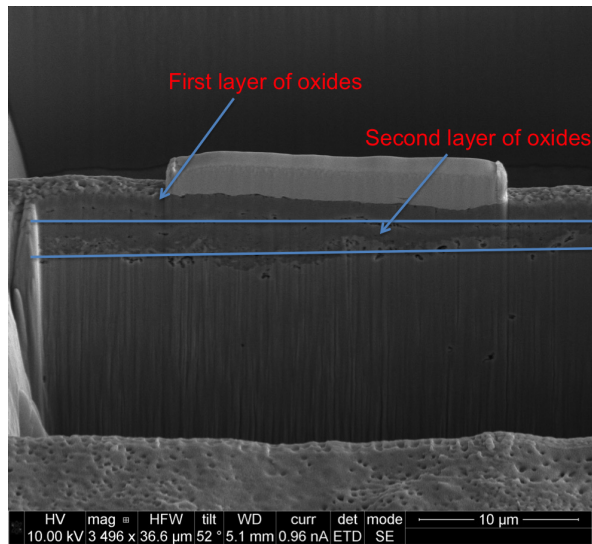


FIG. 25: SEM/FIB image of a TEM specimen being prepared, showing the oxide scale that formed on CGP LTNC AL-6XN after 3.6 ks at 1073 K in air.

destroyed after 3.6 ks at 1073 K in *air* – without even applying steam. The performance of SECIS-treated AL-6XN was somewhat better. Evident from the XRD data in Fig 22, exposure to 1073 K for 3.6 ks in air causes the precipitation of carbides to the extent that the matrix gets completely depleted of carbon. Moreover, the X-ray diffractogram indicates the formation of oxides. This was confirmed by SEM (scanning electron microscopy) and TEM. At the surface of the heat-exposed specimen of Fig 23, the SEM image in Fig 25 reveals a porous oxide layer with a thickness of 3 to 5 μm . The TEM image in Fig 26 resolves two distinct layers within this oxide scale: (i) An outer layer with large grains, mainly a mixture of Fe- and Ni oxides. (ii) An inner layer layer with small grains, mainly chromium oxide.

Apart from local variations caused by carbide precipitates, however, the initial $X_C[z]$ is preserved, as apparent from Fig 24, obtained by exposing CGP LTC AL-6XN to 1070 K for 3.6 ks in *vacuum*. Based on the known mechanism of precipitation hardening, we expect that even after this treatment the alloy surface substantial hardness and wear resistance. Owing to the slight changes in focus in the course of the project (described earlier), SECIS-treated AL-6XN was not exposed to high-temperature steam.

IN-718 performed better than AL-6XN and much better than AISI-316L. Figure 28 shows $X_C[z]$ and $h[z]$ after 3.6 ks at 1073 K under vacuum (red) and in air, respectively. The main difference to the initial $h[z]$ (Fig 8) is a reduction of hardness in a zone $\approx 5 \mu\text{m}$ below the surface. The reason is a corresponding reduction of the carbon fraction X_C within a corresponding zone directly below the surface. Oxidation seems to play no important role here, as the red and the blue graphs are not significantly different. However, the TEM results

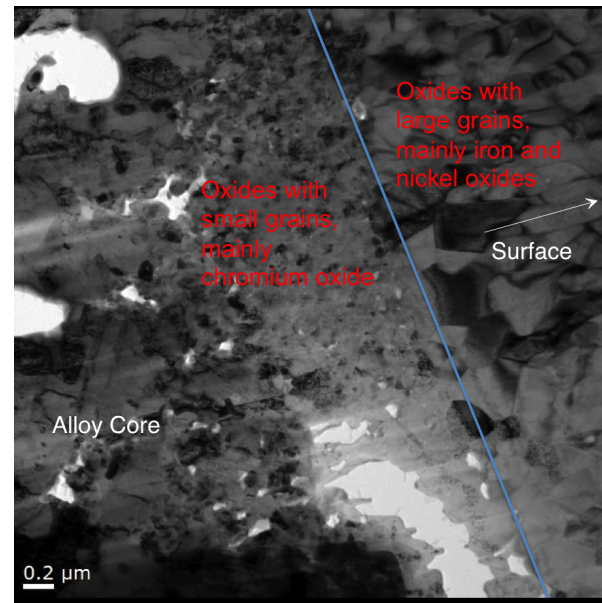


FIG. 26: TEM bright-field image of the oxide scale that formed on CGP LTNC AL-6XN after 3.6 ks at 1073 K in air.

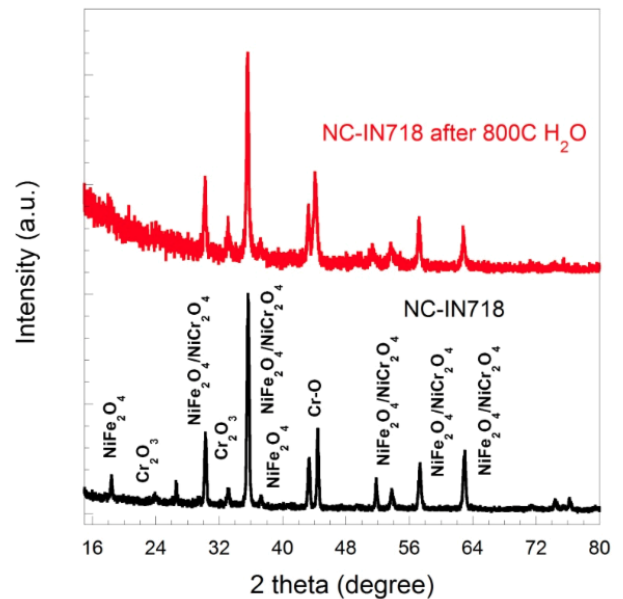


FIG. 27: XRD pattern from LTNC IN-718 after HTSE.

from the specimen treated in air, presented in Fig. 29, do reveal the formation of an oxide layer on the alloy surface. When steam is added to the heat exposure treatment, pronounced formation of oxides does occur, evident from the XRD pattern in Fig 27. Without steam, the thickness of this oxide layer is ranges between 100 and 500 nm. Moreover, the elemental maps indicate that Cr-rich carbide nanoparticles have formed.

This is an important finding, as the major problem with high-temperature heat exposure of IN-718 is the

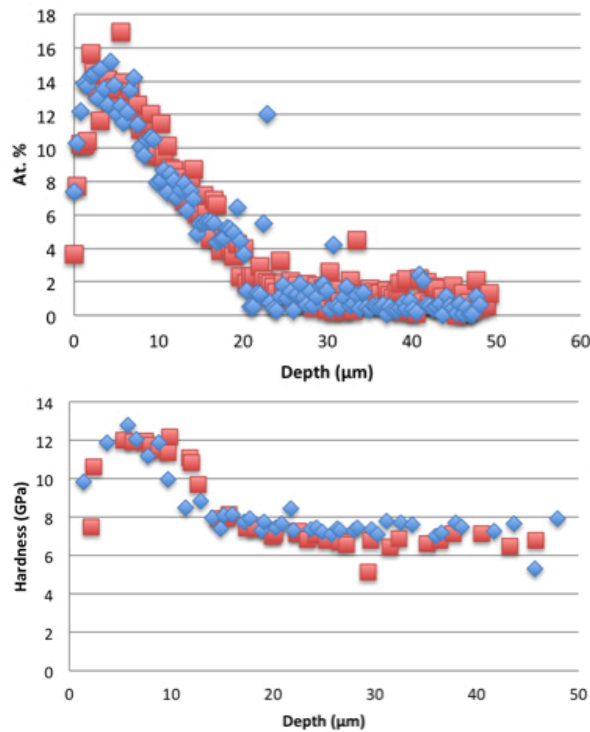


FIG. 28: Heat exposure of CGP LTC IN-718 under simulated accident conditions, 3.6 ks at 1073 K (i) under vacuum (red) and (ii) in air (blue). (a) Carbon-concentration-depth profile $X_C[z]$. (b) Nanohardness-depth profile $h[z]$.

loss of Cr from regions near the surface. Apparently, the high fraction of carbon introduced by LTC is sufficient to bind significant fraction of Cr in Cr-rich carbides. The fine dispersion of carbide particles (hard!) could be one major reason why IN-718 holds up well (and much better than AISI-316L) against HTSE.

Figures 29 are the bright field TEM image and HAADF-STEM image of the 1070 K heat-treated carburized IN-718. Two observations have been made.

H. Irradiation

1. Proton Irradiation

Figure 32 presents results obtained by TEM of CGP LTC AISI-316L after irradiation with 1.5 MeV protons at 620 K. The image at the top left is a STEM (scanning transmission electron microscopy) image showing “Z-contrast” (mass-thickness contrast). Different from the NSE reference specimen irradiated in the exact same way (not shown), Fig 32 shows nanoscopic particles within the grains and lining up along grain boundaries (like pearl strings). The fact that these particles appear darker than the matrix indicates lower mass density. The elemental maps obtained from the region labeled “ROI” by XEDS (X-ray energy-dispersive spectrometry), and in particular those of Cr, Ni, and Fe, indicate that these particles are rich in Cr and low in Fe and Ni. The carbon map does not show any significant

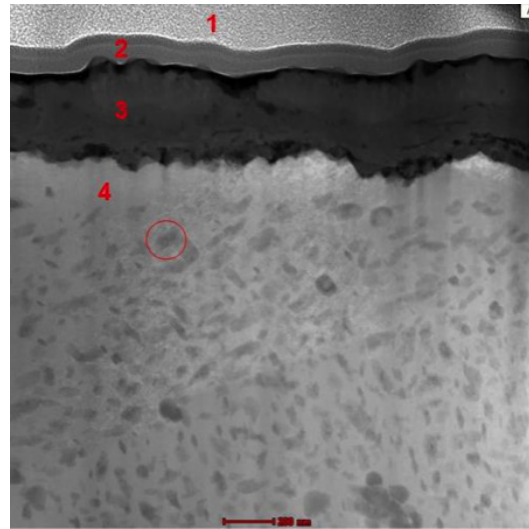


FIG. 29: LTC IN-718 after HTSE: STEM (scanning transmission electron microscopy) image recorded with a HAADF (high-angle annular dark-field detector) detector under conditions producing “Z-contrast” (mass-thickness contrast). Region 1 and 2 are a Pt layer deposited for TEM specimen preparation by FIB. Region 3 is the oxide layer. Region 4 in the carburized zone.

variation, however it is known that XEDS mapping of carbon is problematic. Therefore, the results are not inconsistent with the hypothesis that the nanoscopic particles are Cr-rich carbide precipitates, induced by irradiation.

Apparently, proton irradiation has a similar effect on AISI-316L as HTSE has on IN-718 (Fig. 31): providing mobility to metal atoms (“substitutional” solute atoms), which is suppressed during SECIS, leads to precipitation with a fine (nano-) dispersion of particles. This is understandable recalling that SECIS is a method that provides uniform solid solutions of interstitial atoms with concentrations much higher than the equilibrium solubility limit. Typically (e. g. in CGP LTC AISI-316L), the supersaturation is of order 10^5 , i. e. the concentration of interstitial solute is 100,000 times (!) larger than the equilibrium solubility limit. While precipitation of second phases is kinetically suppressed during processing and normal service life, these solid solutions are fundamentally unstable: A high driving force exists for precipitation of the interstitial solute – or compounds involving it. Under conditions of high driving force and low mobility, e. g. provided by irradiation or heat treatment at moderate temperature, the energy barrier for nucleation of precipitates is small, leading to high number densities of second-phase nuclei, while transport distances are short, limiting the nucleated particles too small size – as experimentally observed.

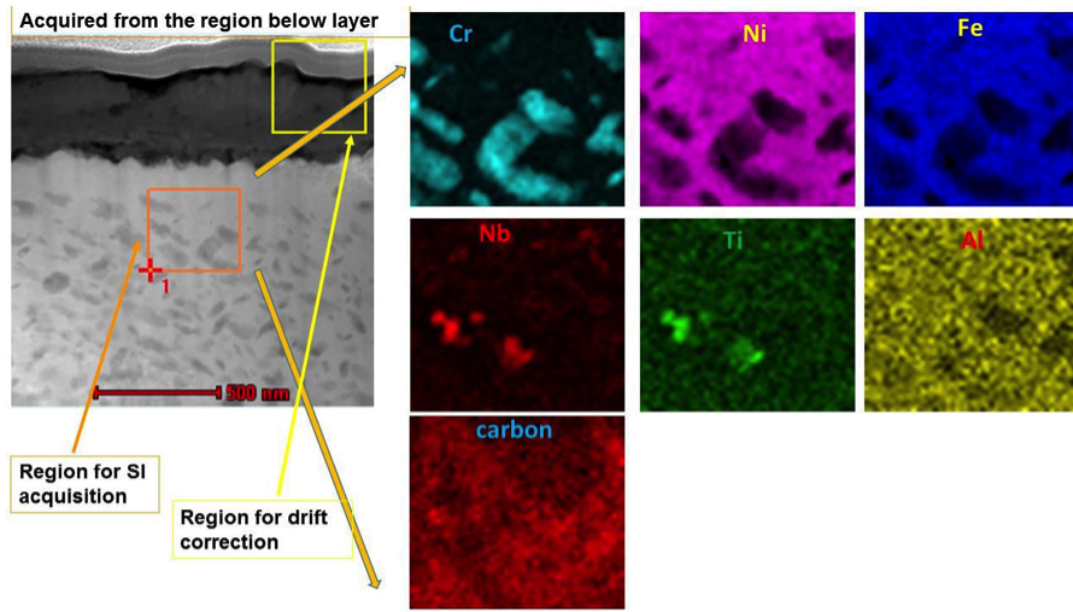


FIG. 30: LTC IN-718 after HTSE: Elemental maps obtained by STEM (scanning transmission electron microscopy) combined with XEDS (X-ray energy-dispersive spectrometry).

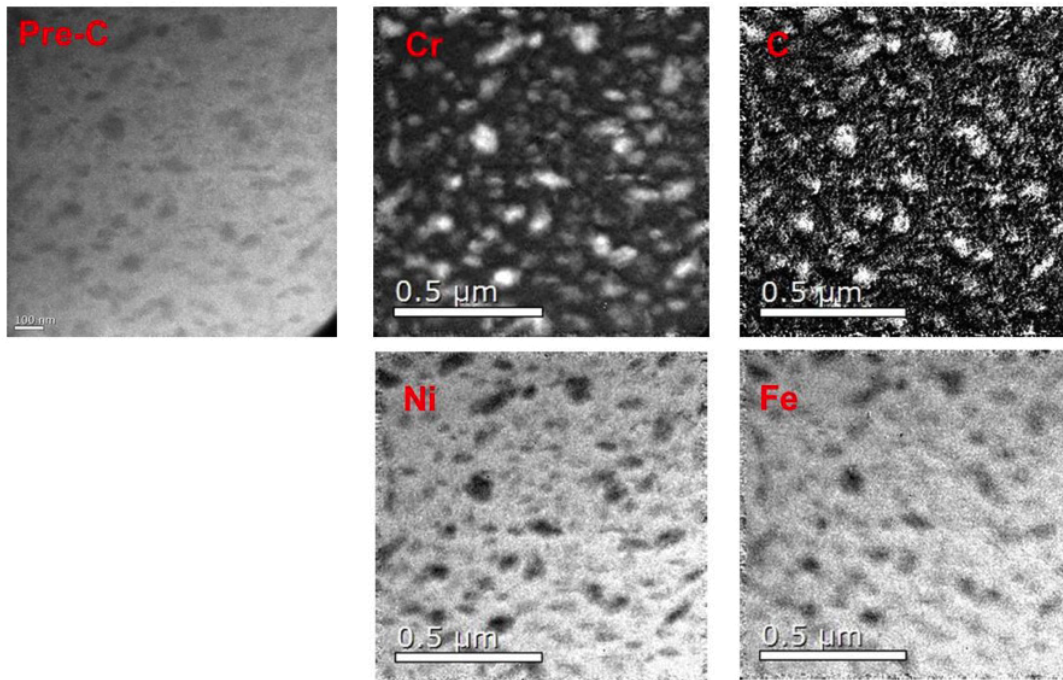


FIG. 31: LTC IN-718 after HTSE: Elemental maps produced by the ESI (electron-spectroscopic imaging) three-window method, an application of EFTEM (energy-filtering transmission electron microscopy).

2. Ni-Ion Irradiation

Figure 33 presents a bright-field TEM image of CGP LTNC IN-718 after irradiation with 5 MeV Ni^{+2} ions. A new layer with a thickness ≈ 100 nm is observed at the surface – presumably an oxide.

Figure 34 and Fig 35 presents DPs (diffraction pat-

terns) that were obtained from Ni-ion-irradiated CGP LTNC IN-718 and from the Ni-ion-irradiated NSE IN-718 reference specimen, respectively. Both patterns show additional spots that can be attributed to precipitates induced by Ni^{+2} ion irradiation in both the nitrocarburized as well as in the non-surface-engineered IN-718.

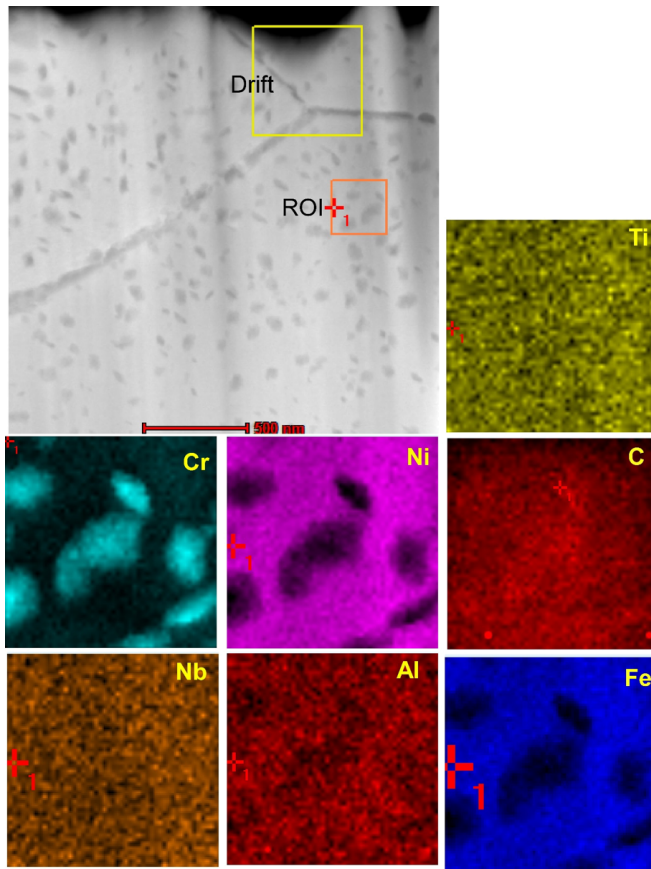


FIG. 32: TEM of CGP LTC AISI-316L after irradiation with 1.5 MeV protons at 620 K. The image at the top left is a STEM (scanning transmission electron microscopy) image showing “Z-contrast” (mass-thickness contrast). The smaller images are concentration-thickness maps of various elements, obtained by XEDS (X-ray energy-dispersive spectrometry) within the region marked by a red square and labeled “ROI” (region of interest) in the main image.

On the other hand, the comparison of the DPs does not indicate any additional effects of LTNC: While Ni^{+2} ion irradiation causes (presumably undesired) phase transformations, these are not caused or promoted by the interstitial solute (carbon, nitrogen).

IV. CONCLUSIONS

1. SECIS was confirmed as a highly effective method for surface engineering of corrosion-resistant (i. e. Cr-containing) alloys.
2. The feasibility of SECIS was demonstrated for variety of structural alloys (AISI-316L, IN-718, AL-6XN) that are of potential interest for nuclear cladding and other applications in nuclear power stations.
3. The CGP method of SECIS was adapted to work with tubes of dimensions used for nuclear cladding.

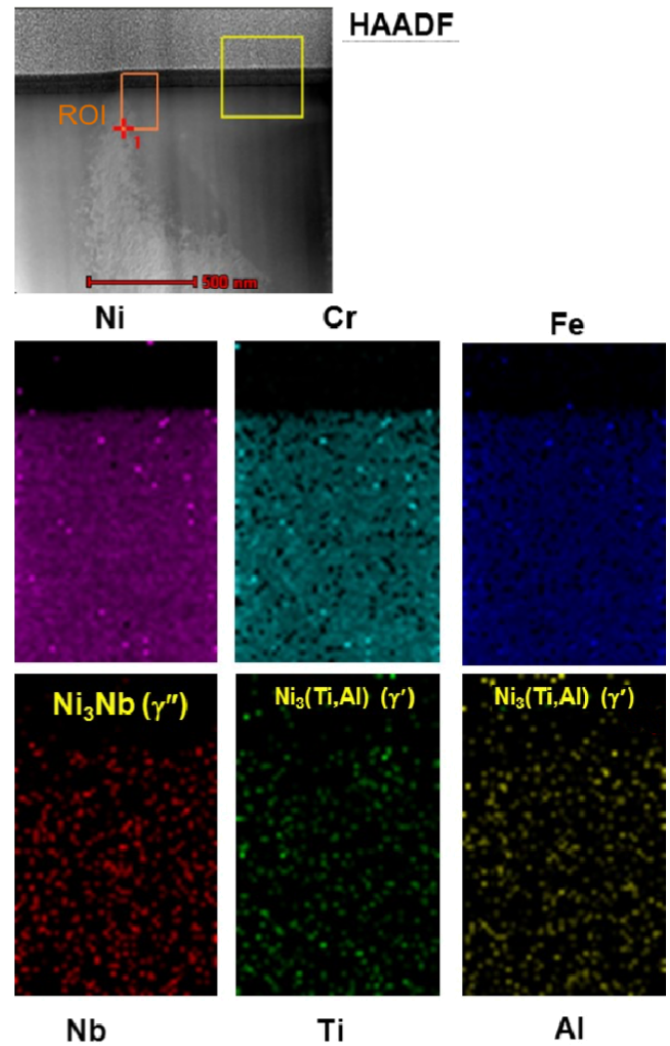


FIG. 33: TEM of CGP LTNC IN-718 after irradiation with 5 MeV Ni^{+2} ions at 620 K. The image at the top left is a STEM image showing “Z-contrast” (mass-thickness contrast). The smaller images are concentration-thickness maps of various elements, obtained by XEDS within the region marked by an orange square in the center of the main image.

4. A new method, based on SRP, was developed and proven to be highly effective in performing LTNC. This method produces a “double case,” which might be beneficial to reduce SCC.
5. A new method of alloy surface activation for SECIS has been discovered filed for patenting. The method relies on external etching in a liquid reagent and temporary passivation against re-oxidation.
6. Systematic and comparative experiments were carried out on SECIS-treated alloys to determine mechanical properties, corrosion resistance, SCC, and impact of irradiation.
7. As a general principle, the presence of a case (hard shell) on an alloy can *reduce* its resistance to SCC. As

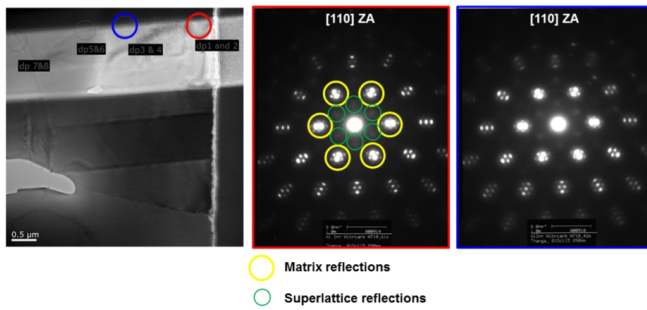


FIG. 34: TEM DPs (diffraction patterns) (and images) of CGP LTNC IN-718 after irradiation with 5 MeV Ni^{+2} ions. Additional reflections (compared to non-irradiated material) indicate irradiation-induced precipitation.

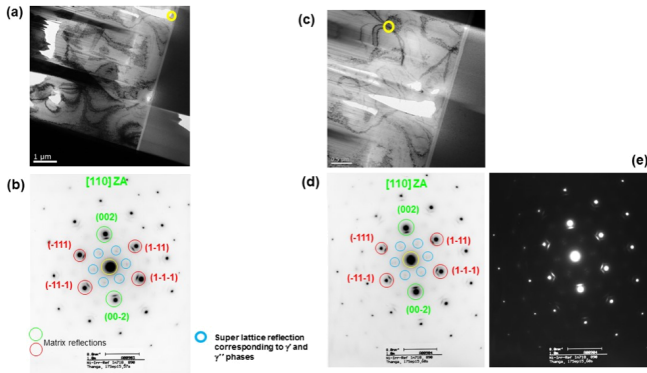


FIG. 35: TEM DPs (diffraction patterns) (and images) of NSE IN-718 reference material after irradiation with 5 MeV Ni^{+2} ions. As in the DPs from the SECIS-engineered specimen of Fig 34, additional reflections (compared to non-irradiated material) indicate irradiation-induced precipitation. Subfigures (d) and (e) are one and the same scanned in different modes to see the superlattice reflections of the precipitates.

harder materials are generally more brittle, a case (hard shell) on a soft alloy core can inject sharp, corrosion-driven cracks into the alloy core.

8. A case formed by SECIS via LTC, LTN, or LTNC is generally under high, GPa-level compressive biaxial residual stresses. As these stresses oppose crack opening, crack formation is not expected in non-strained material or at low tensile strain. However, if large tensile strains are applied – large enough to relax the compressive stress, sharp cracks may form in the case and be injected into the alloy core. In this regime, the material is *more sensitive* to SCC than without SECIS.

9. The surface-engineered layer of all three alloys is sufficiently stable against 24 h exposure to 620 K. Such heat exposure only leads to insignificant changes of the carbon- or nitrogen fraction-depth profile and no precipitation of carbides or nitrides is observed.

10. The most promising material for nuclear applications under normal conditions *and accident conditions*

is IN-718. AISI-316L does not perform well under accident conditions. AL-6XN performs better than AISI-316L, but not as good as IN-718.

11. The case generated on IN-718 by CGP LTNC can be ferromagnetic.

12. Heat exposure of NSE IN-718 under accident conditions causes loss of Cr at the surface and, consequently, rapid oxidation.

13. Treating IN-718 by LTC or LTNC prevents loss of Cr by formation of nanoscopic carbides or nitrides. The nanodispersion of particles is expected to mechanically strengthen the material (compared to NSE IN-718 under the same conditions).

14. Irradiation of AISI-316L with high-energy protons provides diffusivity that can lead to precipitation of nanoscopic Cr-rich carbide particles.

15. Irradiation of IN-718 with high-energy Ni ions can also induce precipitation, however this occurs independently of SECIS.

16. Among the alloys being investigated, IN-718 proved to be the best candidate material for accident-tolerant nuclear fuel cladding: The standard properties of IN-718 can effectively be improved by CGP or SRP or LTC or LTNC. The spatial distribution of interstitial solute is unaffected by longer-term exposure to medium-range temperatures (e. g. 84 ks at 620 K). Exposure to accident-like conditions (4 ks at 1070 K) causes the formation of precipitates that prevent the loss of Cr to the environment and mechanically strengthen the surface region. Irradiation with high-energy ions causes no particular effects in SECIS-treated IN-718 compared to NSE IN-718.

V. ACADEMIC OUTCOMES

1. A productive collaboration was established between the groups at CWRU, UA, and LANL.

2. The PhD thesis of one graduate assistant at CWRU will be entirely based on results from this project.³

3. The results obtained with the new SRP method constitute the basis of a recent MS thesis at CWRU.²

4. At CWRU, three postdoctoral researchers were employed on the project.

5. The work on this project will be a major part of the PhD thesis of a graduate student at UA.⁴

6. One paper has been published on this work, several further papers are in preparation.

-
- ¹ W. Niu, R. S. Lillard, Z. Li, and F. Ernst, *Electrochimica Acta* **176**, 410 (2015).
- ² A. Agaponova, Master's thesis, Case Western Reserve University (2015).
- ³ Z. Li, Ph.D. thesis, Case Western Reserve University (in preparation (2016)).
- ⁴ W. Niu, Ph.D. thesis, University of Akron (in preparation (2016)).